

Supersaturation in the Wake of a Precipitating Hydrometeor and its Impact on Aerosol Activation

Taraprasad Bhowmick^{1,2}, Yong Wang², Michele Iovieno³, Gholamhossein Bagheri², and Eberhard Bodenschatz^{2,4,5}

¹Department of Applied Science and Technology, Politecnico di Torino, Torino, Italy

²Laboratory for Fluid Physics, Pattern Formation and Biocomplexity, Max Planck Institute for Dynamics and Self-Organization, Göttingen, Germany

³Department of Mechanical and Aerospace Engineering, Politecnico di Torino, Torino, Italy

⁴Institute for Dynamics of Complex Systems, University of Göttingen, Göttingen, Germany

⁵Laboratory of Solid State Physics, Cornell University, Ithaca, NY, USA

Key Points:

- This study shows how wake-induced supersaturation in clouds activates aerosols in an equal level of other secondary production processes.
- The parameter space for wake-induced supersaturation behind precipitating spherical hydrometeors is detailed.
- It is described how lucky aerosols are activated in such supersaturated wake of the precipitating hydrometeors.

arXiv:2008.02536v1 [physics.flu-dyn] 6 Aug 2020

Corresponding author: Yong Wang, yong.wang@ds.mpg.de

Corresponding author: Gholamhossein Bagheri, gholamhossein.bagheri@ds.mpg.de

Abstract

The secondary activation of aerosols impacts the life cycle of a cloud. A detailed understanding is necessary for reliable climate prediction. Recent laboratory experiments demonstrate that aerosols can be activated in the wake of precipitating hydrometeors. However, many quantitative aspects of this wake-induced activation remain unclear. Here, we report a detailed numerical investigation of the activation potential of wake-induced supersaturation. By Lagrangian tracking of aerosols we show that a significant fraction of aerosols are activated in the supersaturated wake. These ‘lucky aerosols’ are entrained in the wake’s vortices and reside in the supersaturated environment sufficiently long to be activated. Our analyses show that wake-induced activation can contribute at a level similar to other well known secondary production processes.

Plain Language Summary

We numerically investigate how new water droplets or ice particles are formed within a cloud. Out of several proposed physical processes for droplet generation, recent experimental studies have shown that a large droplet can nucleate aerosols in the wake behind it when falling under gravity. We present a detailed analysis of various physical factors that lead to an excess of water vapor behind the hydrometeors (e.g., droplets, sleet or hail) and investigate the effectiveness of this process on activation of aerosols to create new cloud particles.

1 Introduction

The dynamics of atmospheric clouds remains a major source of uncertainty in weather and climate models (Stevens & Bony, 2013) due to the interplay of many physical processes over a wide range of scales (Bodenschatz et al., 2010). Especially the activation of aerosols and species therein controls the lifetime of a cloud (Kreidenweis et al., 2019) in which fractions of cloud condensation nuclei (CCN) and ice nucleating particles (INP) develop into new hydrometeors (M. B. Baker, 1997). Physical processes contributing to the activation (Field et al., 2017) within a mature cloud can not explain the observed discrepancies between the measured activation and the observed hydrometeor population, which is several orders of magnitude higher than expected (Pruppacher & Klett, 2010; Y. Huang et al., 2017). One possible explanation of this riddle might be the recently discovered wake-induced supersaturation and activation of aerosols behind large precipitating hydrometeors, i.e. heterogeneous wake-induced nucleation (Prabhakaran et al., 2017; Chouippe et al., 2019; Prabhakaran et al., 2020). The experimental investigation by Prabhakaran et al. (2017) of falling drops (diameter of $\mathcal{O}(1)$ mm) in near critical point conditions of pressurized sulfur-hexafluoride showed evidences of homogeneous nucleation in the wake. Prabhakaran et al. (2020) conducted a follow-up experiment on heterogeneous nucleation using sodium chloride and silver iodide aerosols under atmosphere-like conditions. Warm droplets with a diameter of ~ 2 mm were able to induce the activation of ice aerosols in their wake when precipitating through a subsaturated colder environment. Earlier, a numerical analysis of supersaturation in the wake of a warmer hydrometeor moving through various colder environments was performed by Chouippe et al. (2019). Their work confirms the existence of a supersaturated region in the wake of a hydrometeor that settles through a colder saturated environment. The maximum supersaturation observed in the wake was higher the larger the temperature difference between the hydrometeor and the ambient was. In a more recent study, Krayer et al. (2020) extended their earlier work Chouippe et al. (2019) and explicitly estimated the influence of wake supersaturation on the ice enhancement factor using a model based on a power law dependence of the local supersaturation (Huffman, 1973; B. A. Baker, 1991) and concluded that the local ice nucleation enhancement alone cannot produce a sufficient number of activated ice nuclei to solve the observed number discrepancy. Although the development of supersaturation was studied numerically, the direct calculation of nucleation remained quite

difficult due to the large number of parameters that include size distribution (Dusek et al., 2006), number concentration (M. B. Baker, 1997), chemical composition (Curtius, 2009; DeMott et al., 2018), porosity or solubility (Kanji et al., 2017) of aerosols etc. The complexity in the nucleation of aerosols is further complicated in mixed-phase clouds containing both water and ice phase hydrometeors. Ice nucleation through deposition and condensation freezing can occur on an aerosol during supersaturation in the ice phase at sub-zero temperatures (Meyers et al., 1992). Activation of aerosols by immersion freezing on a CCN or by contact freezing on a supercooled water drop can also be observed (Kanji et al., 2017).

The above mentioned studies elucidated some aspects of wake supersaturation and aerosol initiation. In this letter, we present a comprehensive numerical study covering the parameter space relevant for atmospheric situations. We quantify the influence of ambient humidity and ambient/hydrometeor temperatures on the supersaturation within the wake for different sizes and phases of spherical hydrometeors. Next, with Lagrangian tracking of aerosols as passive tracers around such sedimenting hydrometeors we quantify the residence time and supersaturation experienced by individual aerosols as a function of the governing parameters. Finally, we discuss how these results can help to quantify the likelihood and significance of heterogeneous wake-induced nucleation in atmospheric clouds.

2 Model and Methods

We numerically simulate the flow around a solid spherical hydrometeor with diameter d_p and temperature T_p falling in air (ambient: temperature T_∞ , relative humidity RH_∞ , density ρ_a and pressure p_∞) with constant velocity U_p . While in general the shape of the hydrometeor will not be spherical and solid we expect this to be a good approximation. In the simulation all parameters are assumed to be constant, as the hydrometeor’s and environment’s properties vary slowly compared to that of the momentary flow (for more details see supporting information S2 and S3).

In dimensionless form the incompressible Navier-Stokes (NS) equations and the one-way coupled advection-diffusion (AD) equations for temperature and water vapor density are,

$$\nabla \cdot \mathbf{u} = 0, \quad (1)$$

$$\frac{\partial \mathbf{u}}{\partial t} + \mathbf{u} \cdot \nabla \mathbf{u} = -\nabla p + \frac{1}{Re} \nabla^2 \mathbf{u}, \quad (2)$$

$$\frac{\partial T}{\partial t} + \mathbf{u} \cdot \nabla T = \frac{1}{Re Pr} \nabla^2 T, \quad (3)$$

$$\frac{\partial \rho_v}{\partial t} + \mathbf{u} \cdot \nabla \rho_v = \frac{1}{Re Sc} \nabla^2 \rho_v. \quad (4)$$

where p is the dimensionless pressure $(p - p_\infty)/\rho_a U_p^2$, $Re = U_p d_p/\nu$ is the Reynolds number (with ν being the kinematic viscosity of air), $Pr = \nu/\kappa$ is the Prandtl number (with κ being the thermal diffusivity of air), $Sc = \nu/\kappa_v$ is Schmidt number (with κ_v being the water vapor diffusivity). Following Kotou et al. (2009) and Krayner et al. (2020), as a first approximation, we neglect evaporation feedback on the momentum and particle temperature in the simulations(see S4).

We solve the model equations with the lattice Boltzmann method (LBM) (Succi, 2001; Qian et al., 1992; Guo et al., 2002; Silva & Semiao, 2012; Krüger et al., 2017; Tian et al., 2018) within the open-source LBM library Palabos (Latt et al., 2020). The simulation domain, with reference frame in the center of the hydrometeor, extends $[-5, 20]d_p \times [-3.5, 3.5]d_p \times [-3.5, 3.5]d_p$ with a uniform Cartesian mesh of grid size $d_p/32$. The surface of the hydrometeor is no-slip at zero velocity and with a constant temperature T_p and water vapor density $\rho_{v,p} = \rho_{vs}(T_p)$ which is saturated at T_p according to Maxwell diffusion model.

3 Results

We analyze the flow at different Reynolds numbers in the steady axisymmetric wake ($0 \leq Re \leq 220$) and in the steady oblique wake ($225 \leq Re \leq 285$) (see Johnson and Patel (1999), and Tomboulides and Orszag (2000)), with $Pr = 0.71$ and $Sc = 0.61$ according to the values of the atmospheric standard conditions (Montgomery, 1947; Michaelides, 2006). In the case of a liquid hydrometeor of density 10^3 kg m^{-3} this corresponds to a particle with a diameter between $3 \times 10^{-4} \text{ m}$ and $1.03 \times 10^{-3} \text{ m}$ falling with terminal velocities between 1.21 m s^{-1} and 4.03 m s^{-1} . The ambient relative humidity RH_∞ is varied from nearly saturated ($RH_\infty \sim 100\%$) within the cloud (Siebert & Shaw, 2017) to a highly subsaturated in the open atmosphere (see also Prabhakaran et al. (2020)). The supersaturation $S = RH - 1 = \rho_v/\rho_{vs}(T) - 1$ is computed with respect to the water phase when $T > 0^\circ\text{C}$ and with respect to the ice phase when $T \leq 0^\circ\text{C}$ by using the following empirical Equations (5) and (6) for liquid and frozen hydrometeors respectively (J. Huang, 2018).

$$\rho_{vs}(T)_{(T>0^\circ\text{C})} = \frac{1}{R_v(T + 273.15)} \frac{\exp(34.494 - 4924.99/(T + 237.1))}{(T + 105)^{1.57}}, \quad (5)$$

$$\rho_{vs}(T)_{(T\leq 0^\circ\text{C})} = \frac{1}{R_v(T + 273.15)} \frac{\exp(43.494 - 6545.8/(T + 278))}{(T + 868)^2}. \quad (6)$$

We identify each simulations with a defined nomenclature, like for example, ‘LC 0 15 90’. Here the first letter indicates the hydrometeor phase (L liquid or I ice), the second letter indicates the sign of the temperature difference between the hydrometeor and the ambient (W warmer hydrometeor or C colder hydrometeor), and the three following numbers give the hydrometeor temperature T_p (in degrees Celsius), the modulus of $T_p - T_\infty$ referred as ΔT (in degrees Celsius) and the ambient relative humidity RH_∞ (in %). Thus, ‘LC 0 15 90’ is a liquid hydrometeor colder than the ambient, with a surface temperature of 0°C in an ambient air with a temperature of 15°C and a relative humidity equal to 90%.

3.1 Supersaturation in the wake

Figure 1(a) shows an example of a visualization of the supersaturation field at $Re = 275$ in an ambient relative humidity of 90% with respect to ice phase for a warm hydrometeor (IW 0 15 90). High supersaturation is clearly visible in the boundary layer of the droplet and in the near wake, as well as, in the large region downstream of the hydrometeor. In this oblique regime, some streamlines pass through the wake’s vortices, a feature consistent with the results of Johnson and Patel (1999) for the oblique wake vortex structures. The overall distribution of supersaturation in the entire three dimensional domain above a supersaturation threshold of $S_0 > 1 \times 10^{-4}$ is shown in Figure 1(b). There the supersaturation spectrum $Sp(S)$ is normalized by the hydrometeor volume and the supersaturated volume $V_S = \int_{S_0}^{S_{max}} Sp(S) dS$ is an integral of $Sp(S)$. To avoid numerical round-off errors around the surface of the hydrometeor, where $S = 0$, the supersaturation threshold is defined as 1×10^{-4} , with S_{max} being the maximum supersaturation obtained in a simulation. The statistics of the bright colored supersaturated region in Figure 1(a) shows the evolution $\propto S^{-2}$ in Figure 1(b). The trend of S^{-2} ceases around $S \geq 0.13$, which is the highest magnitude of S reached within the boundary layer and in the recirculating zone behind the hydrometeor in Figure 1(a). $Sp(S)$ decreases slightly with increasing Reynolds number, which implies a reduction in the volume of the supersaturated region with respect to the hydrometeor volume, due to gradual thinning of the boundary layer and a correlated shrinking of the lateral extent of the wake. Although a volumetric change in V_S is observed with different Re , the magnitudes of S_{max} remain almost constant for a specific thermodynamic state, independent of Re .

The evolution of V_S as a function of Re and other thermodynamic parameters is shown in Figure 2(a) for exemplary cases presenting a temperature difference ΔT of 15°C and $RH_\infty = 95\%$. For full details on the evolution of V_S in a whole range of Re , ΔT , RH_∞ ,

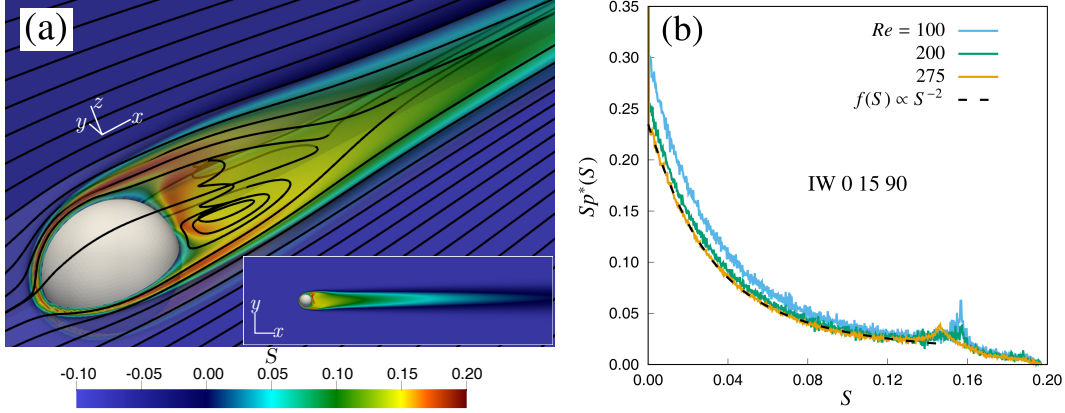


Figure 1. Spatial distribution of S . (a) Contours of S in two orthogonal central planes and complex streamlines for $Re = 275$. Only the region near the hydrometeor is plotted, while the entire two dimensional domain along the orthogonal (x, y) plane is in the inset. (b) Normalized sample population spectrum $Sp^*(S) = Sp(S)/(\pi d_p^3/6)$ for various magnitudes of supersaturation ($S > 0$) over the entire three dimensional domain for the case ‘IW 0 15 90’ for the $Re = 100, 200$ and 275 . ‘IW 0 15 90’ represents an (I) frozen but (W) warmer hydrometeor with (0) $T_p = 0^\circ\text{C}$ in an ambient at $T_\infty = -15^\circ\text{C}$, which gives (15) $\Delta T = 15^\circ\text{C}$ and (90) $RH_\infty = 90\%$ with respect to the (I) ice phase.

hydrometeor phase (I or L), and warmer (W) or cooler (C) setups, see S5. In general, a frozen hydrometeor (solid lines) produces a significantly larger supersaturated region than a liquid hydrometeor (dashed lines). This is partly due to the lower magnitude of the saturation vapor pressure in the ice phase compared to its magnitude in the liquid water phase at temperatures of $< 0^\circ\text{C}$ (e.g., 13.7% lower at -15°C). The evolution of V_S , as shown in Figure 2(a), with respect to the hydrometeor phase and its warmer or colder state also applies to all other ΔT and RH_∞ , as detailed in the supporting information. Figure 2(a) also shows that warmer liquid droplets, as for example, ‘LW 15 15 95’ in $T_\infty = 0^\circ\text{C}$ produce almost 2.3 – 2.5 times larger V_S than ice hydrometeors like ‘IC -15 15 95’. This is generally true also for other ΔT and RH_∞ . This signifies that the warmer hydrometeors produce larger V_S than the colder ones for similar T_∞ , ΔT and RH_∞ . This phenomenon can be further explained by analytically solving the normalized T and ρ_v equations (see S6) for $Re \sim 0$, where warmer liquid droplets like ‘LW 15 15 RH_∞ ’ also produce larger V_S than the colder frozen hydrometeors as ‘IC -15 15 RH_∞ ’ for various RH_∞ conditions. It is further observed that a minimum of $\Delta T = 4 - 10^\circ\text{C}$ is necessary to produce $V_S \sim \mathcal{O}(1) \times \pi d_p^3/6$, which are merely thin supersaturated boundary layers around the hydrometeor. For hydrometeors that are colder than the ambient, ΔT needs to be at least $6 - 12^\circ\text{C}$ to produce a similar volume of V_S .

In all cases, the supersaturated volume can be fitted by the following scaling function (goodness of fit 99.8%) for the whole range of the Reynolds number, despite the change in the wake structure around $Re = 220$.

$$V_S = C_0(1 + C_1 Re^\alpha) \quad (7)$$

The fitting coefficient C_0 represents an asymptotic value, which depends on the thermodynamic parameters of the ambient and the hydrometeor, i.e., ΔT , RH_∞ , (I) ice or (L) liquid, (W) warm or (C) colder temperature than the ambient. The coefficient C_1 and the exponent α show a minor sensitivity to the thermodynamic parameters, as, C_1 is between 10 – 13 and α is -0.63 ± 0.02 for our simulations. The data only deviates significantly

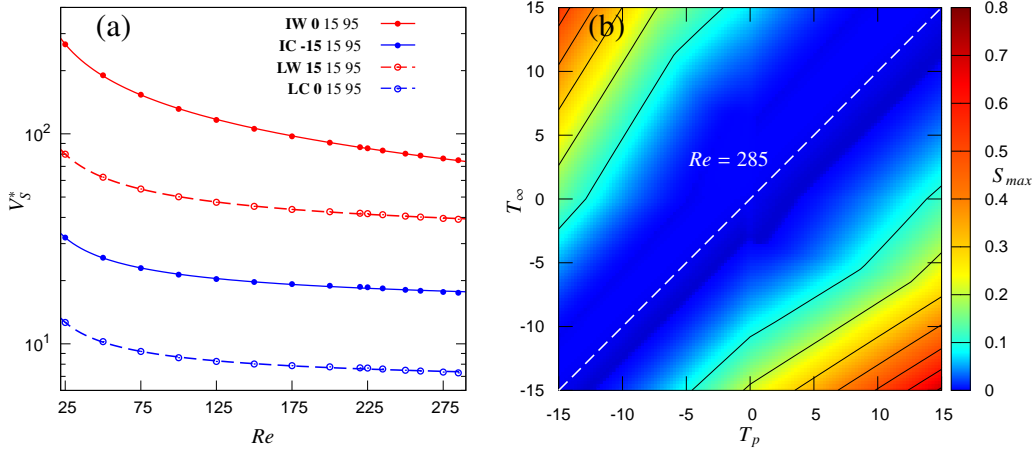


Figure 2. The evolution of supersaturation in the wake. (a) The supersaturated volume $V_S^* = V_S/(\pi d_p^3/6)$ is plotted against different Re , considering both (I) frozen and (L) liquid hydrometeors with both (W) warmer or (C) colder temperature than the ambient, while maintaining $\Delta T = 15^\circ\text{C}$ and $RH_\infty = 95\%$. The dots are simulation results, while the lines correspond to the $C_0(1 + C_1 Re^\alpha)$ fitting model. Solid dots/lines represent frozen hydrometeors and the empty dots/dashed lines represent liquid hydrometeors, with red and blue color for warmer and colder hydrometeors respectively. (b) Supersaturation maximum S_{max} for different values of T_p and T_∞ varying from -15 to 15°C for $Re = 285$ keeping $RH_\infty = 95\%$. Black contour lines are drawn for each 0.1 increase in S_{max} .

when the supersaturated region is not completely within the computational domain (e.g., the case of warmer ice hydrometeors at higher Reynolds number and in almost saturated ambient) and we thus consider this a numerical artifact. We observed that the $Re^{-0.63}$ scaling of the supersaturated volume closely follows the scaling of the drag coefficient with the Reynolds number in the investigated range of Re (Clift et al., 1978). Thus the decrease in V_S follows the dynamics of the wake, as also Figure 1(a) suggests. This aspect requires, however, further quantitative investigation.

Figure 2(b) shows the development of the maximum supersaturation S_{max} over a wide range of hydrometeor temperature T_p and ambient temperature T_∞ at a fixed Reynolds number $Re = 285$ and an ambient relative humidity $RH_\infty = 95\%$ for both (I) frozen and (L) liquid hydrometeors with both (W) warmer or (C) colder temperature than the ambient. The diagonal in white dashed line corresponds to $T_p = T_\infty$ and divides the plane into the colder hydrometeor case (top left) and the warmer hydrometeor case (bottom right). The temperature difference ΔT plays a crucial role, since S_{max} increases almost exponentially with it at constant RH_∞ . Similar to V_S , warmer hydrometeors generally produce a higher supersaturation maximum than colder hydrometeors at the same ΔT , regardless of their frozen or liquid state. The only exception happens in a nearly saturated ambient at $T_\infty = 0^\circ\text{C}$, because the warmer hydrometeor is a liquid one while the colder one is frozen. In addition, S_{max} evolves almost independently of Re for various thermodynamic conditions. For details see S7.

3.2 Residence time of aerosols in the wake

Atmospheric aerosols, which can be activated as CCN or INP, behave as passive tracers due to their negligible Stokes number. To understand the possible role of the supersaturated hydrometeor wake on the aerosol activation, we have analyzed the trajectories of passive

tracers injected upstream of the hydrometeor. Since only tracers starting their motion near the center line $y = z = 0$ can enter the supersaturated regions, two injection patterns are used: a coarse pattern where 2601 tracers are injected uniformly over an area of $[1.5d_p \times 1.5d_p]$ and a fine pattern where 1681 tracers are injected uniformly over an area of $[0.2d_p \times 0.2d_p]$ in the inlet around the hydrometeor center line. An adaptive Runge-Kutta 4-5 method is used for time integration of the trajectories. Velocity, temperature and vapor density at the tracer position are obtained by tri-linear interpolation.

The possibility of an aerosol being activated as a CCN or an INP depends both on the instantaneous supersaturation it experiences and on the time it spends in highly supersaturated regions (residence time), so that it reaches a critical size that prevents its complete evaporation/sublimation according to the Köhler curve (Seinfeld & Pandis, 2006). In Figure 3 we therefore plot the residence time τ_S that a tracer spends within the supersaturated wake in panels (a) and (b), and S_{max} that it sees in (c) and (d) as a function of the initial radial distance r of the tracer from the hydrometeor center line for axisymmetric ($Re = 200$) and oblique ($Re = 285$) wakes, respectively. The different structure of the wake creates clearly visible differences in the supersaturation experienced by the tracers. The tracers, which stay for the longer time in the supersaturated region of axisymmetric $Re = 200$ wake, are introduced near the center line as shown in Figure 3(a), so that they move through the supersaturated boundary layer and along the border of the wake. However, no tracers could enter the closed recirculating region, resulting τ_S at most in the order of $10^1 d_p/U_p$ for $Re = 200$.

In the oblique wake regime of $Re = 285$, shown exemplary in Figure 3(b), tracers injected far from the axis show no significant qualitative difference in τ_S and they experience lower S_{max} in Figure 3(d) for a short time. However, ‘lucky tracers’ injected near the center line can enter the near wake vortical region and therefore remain trapped in the supersaturated recirculating zone for a longer time before moving downstream. This increases τ_S by a factor between 2.5 to 9 with respect to the bulk of the tracers injected from the same radial distance in the symmetric or oblique wake regimes. We quantify the extent of the injection region of lucky tracers with $\tau_S \geq 10^2 d_p/U_p$, which is confined to a radial distance of $r/d_p \leq 0.09$. The ‘capture efficiency’ E , which is defined as the ratio between the total frontal area A_F of the tracers with $\tau_S \geq 10^2 d_p/U_p$ and the frontal area of the hydrometeor $\pi d_p^2/4$, is about 5×10^{-3} for $Re = 285$, while it is almost zero in the steady axisymmetric regime. The scatter in Figure 3(b) for $Re = 285$, which produces petal-like patterns at low r/d_p , is due to the lack of axial symmetry in the oblique wake regime. The larger extent of the supersaturated region generated by a warmer hydrometeor (solid dots) compared to a colder hydrometeor (empty dots) for the same ΔT and RH_∞ is also visible in Figure 3. This is evident from the lower decay of τ_S and S_{max} with r/d_p for warmer hydrometeors.

The mechanism allowing long residence times in the case of an oblique wake can be inferred from Figure 3(e), which shows two sample tracer trajectories with $r/d_p = 0.078$ and 0.066, respectively, each of which enter the vortical oblique wake region at $Re = 285$. The colors of the trajectories represent the instantaneous supersaturation the tracers experience. Such lucky tracers, introduced very near the hydrometeor center line, experience a sudden maximum of supersaturation $S \sim 20\%$, for a short time as they move through the boundary layer on the front of the sphere. Then the supersaturation gradually decreases along the trajectory to about 10%. Later, when the tracer is entrained within the recirculating oblique wake zone, it experiences higher supersaturation again, but for a longer time due to the low velocity and complex three dimensional flow structures of this region. However, such entrainment phenomenon is only observed when the wake loses its symmetry, i.e. in the oblique wake regime from $Re = 225$ in our simulations.

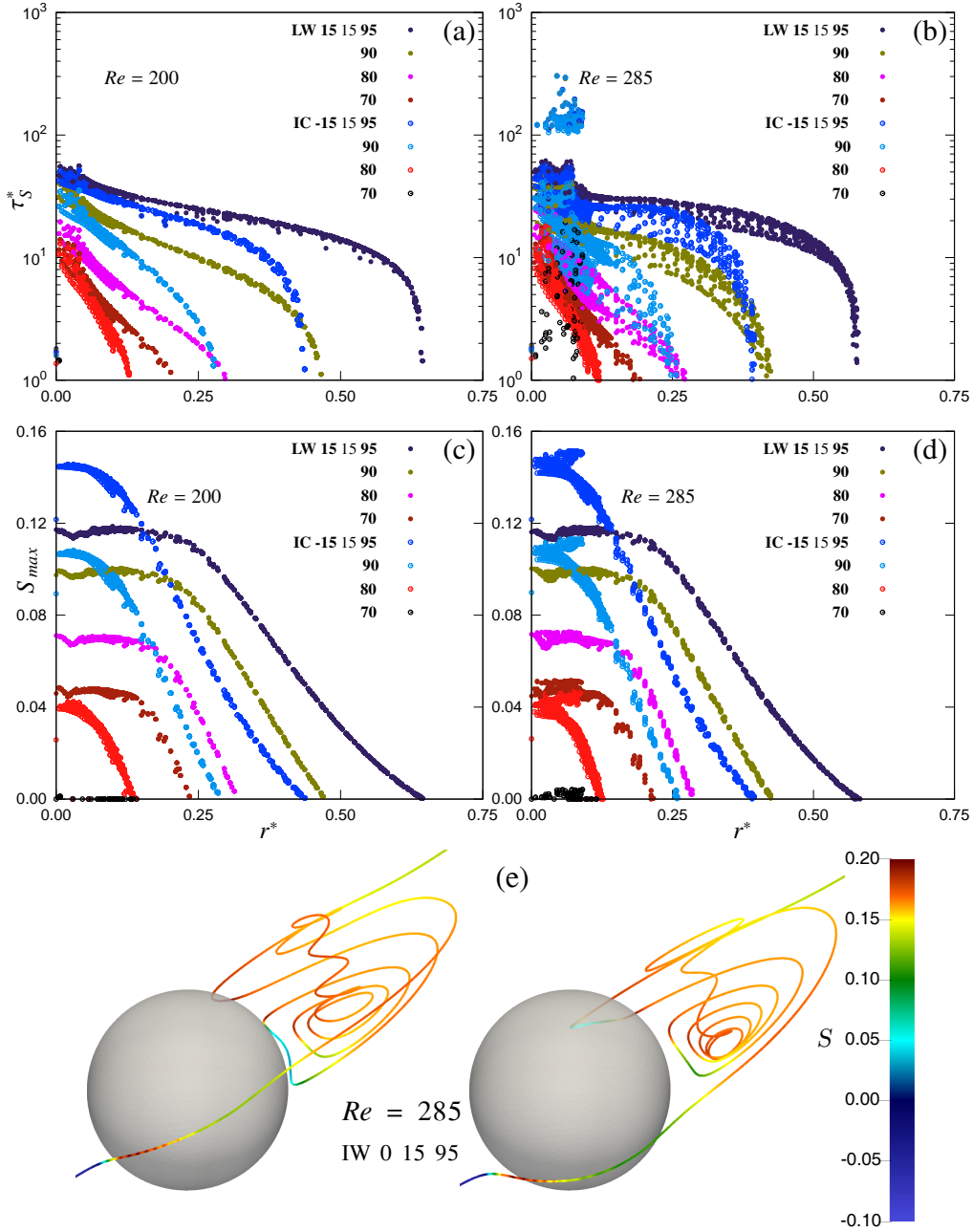


Figure 3. The residence time $\tau_S^* = \tau_S/(d_p/U_p)$ of a tracer within the supersaturated zone and the maximum supersaturation S_{max} experienced by a tracer are plotted as a function of the initial radial distance $r^* = r/d_p$ from the hydrometeor center line ($y = z = 0$). The evolution of τ_S^* within the $S > 1 \times 10^{-4}$ zone is plotted for $Re = 200$ in (a) and for $Re = 285$ in (b), while S_{max} is plotted for $Re = 200$ in (c) and for $Re = 285$ in (d). Various hydrometeor phases and RH_∞ conditions are considered keeping $\Delta T = 15^\circ\text{C}$ and $T_\infty = 0^\circ\text{C}$. Solid and empty dots represent the liquid warm and frozen cold hydrometeor conditions, respectively. In (e), two example tracer trajectories for $Re = 285$ are shown, colored according to the instantaneous S it experiences in an ‘IW 0 15 95’ setup, resulting in $\tau_S^* = 151$ s (left) and $\tau_S^* = 145.4$ s (right).

4 Implications for the Nucleation in Clouds

The extent of the supersaturated volume, the maximum supersaturation and the residence time of an aerosol in the supersaturated wake of precipitating hydrometeors provide important insights on aerosol activation in the atmosphere. For the aerosol entrainment in the wake, the precipitating hydrometeor has to generate an oblique wake, which occurs for a precipitating spherical raindrop when the diameter is at least 1 mm. Since raindrops exceeding a diameter of 2 to 3 mm are very rare and occur mostly in thunderstorms (Pruppacher & Klett, 2010), and also to satisfy the need for higher temperature difference; it is evident that wake-induced supersaturation can happen mainly in deep convective clouds with fully glaciated, mixed phased as well as various liquid phase hydrometeors due to a large temperature variation (Yuan et al., 2010). From the results of the previous section, the entrainment rate of ‘lucky aerosols’, which enter per unit time into the frontal capture area A_F of a hydrometeor and thus experience a long residence time inside the supersaturated wake, is estimated as

$$N = N_a U_p A_F = N_a U_p E \pi d_p^2 / 4.$$

Here E is the capture efficacy, which is about 5×10^{-3} for $Re = 285$ and almost zero in the steady axisymmetric regime. N_a is the typical aerosol concentration, which varies from $\mathcal{O}(10^8)$ to $\mathcal{O}(10^9)\text{m}^{-3}$ within the continental clouds, and from $\mathcal{O}(10^7)$ to $\mathcal{O}(10^8)\text{m}^{-3}$ within the remote marine clouds (Pruppacher & Klett, 2010). Therefore, $\mathcal{O}(10^0)\text{s}^{-1} \leq N \leq \mathcal{O}(10^1)\text{s}^{-1}$ aerosols in continental clouds and $\mathcal{O}(10^{-1})\text{s}^{-1} \leq N \leq \mathcal{O}(10^0)\text{s}^{-1}$ aerosols in remote marine clouds experience a higher residence time and higher supersaturation in the wake when a raindrop of at least 1 mm diameter settles at its terminal velocity ($Re \simeq 285$). Measurements of the number density of raindrops above 1 mm show a wide variability, which can be estimated to be in the range of $\mathcal{O}(10^1) - \mathcal{O}(10^2)$ drops per cubic metre (e.g., Waldvogel, 1974; Adirosi et al., 2016, and others). This leads to an entrainment rate of aerosols in the drop wakes between $\mathcal{O}(10^0)$ and $\mathcal{O}(10^3)\text{m}^{-3}\text{s}^{-1}$. Since the capture efficiency E increases with the Reynolds number (we use the E of $Re = 285$), this could be considered a conservative estimate.

The critical supersaturation required for activation of aerosols is achieved by solving the Köhler equation for its chemical compositions and size (e.g., Seinfeld & Pandis, 2006; McFiggans et al., 2006; Lohmann, 2015, and others). Since critical supersaturation needed for the heterogeneous nucleation of common atmospheric aerosols rarely exceed 1 – 2% in a uniform environment, we may estimate the aerosol growth (see S8) during its residence time within the supersaturated wake by considering the average supersaturation, which is much higher than 2% for a temperature difference of 15 °C between the hydrometeor and the ambient. Such estimation shows that inside such a supersaturated wake, an aerosol can grow well above its critical radius and therefore be activated. During a convective precipitation process of typically 20 minutes, $\mathcal{O}(10^3) - \mathcal{O}(10^6)\text{m}^{-3}$ new aerosols can therefore be activated in the wake of the precipitating hydrometeors, which replenish the activated particle concentration in clouds that typically vary in $\mathcal{O}(10^8) - \mathcal{O}(10^9)\text{m}^{-3}$ (Rosenfeld et al., 2016). This rate of secondary activation is well comparable with the experiment of Mossop (1976) on secondary ice production during the growth of a graupel by rimming splintering and with the in cloud measurements of secondary ice particles by Heymsfield and Willis (2014). However, for an explicit quantification of wake-induced nucleation, a detailed micro-physical study is required taking into account the full details of the changing atmospheric conditions and the particle evolution while falling through the convective cloud. In addition, the effects of other influencing factors, such as cloud free stream turbulence (Bagchi & Kottam, 2008), strong convective motions like central updraft or entrainment induced mixing (e.g., Grabowski & Wang, 2013; Nair et al., 2020; Bhowmick & Iovieno, 2019, and others), or strong downdraft during precipitation (Wang et al., 2016) may further influence this nucleation and activation rate, which needs to be carefully investigated.

5 Summary and Concluding Remarks

In this letter a detailed analysis of the supersaturation field and aerosol activation around a spherical hydrometeor, which settles at its terminal velocity, for different atmospheric conditions is presented. The Navier-Stokes equation for the flow velocity and the one-way coupled advection-diffusion equations for temperature and density of water vapor are solved with the lattice Boltzmann method. The supersaturated volume V_S in the wake of steady axisymmetric regime ($Re \leq 220$) and oblique regime ($225 \leq Re \leq 285$) shows a $Re^{-0.63}$ decrease for the same thermodynamic conditions. Whereas, V_S is very sensitive to the temperature difference ΔT between the hydrometeor and the ambient and its relative humidity condition RH_∞ , so that V_S at constant ΔT increases as RH_∞ increases, which means that a small amount of vapor diffusion from a warmer hydrometeor or cooling by a colder hydrometeor can easily supersaturate an almost saturated wake volume. However, when RH_∞ is fixed, ΔT plays a crucial role in V_S , since without an adequate ΔT a negligible supersaturated volume is generated. In addition, persistently warmer hydrometeors than the ambient produced larger V_S than the colder ones. The supersaturation maximum S_{max} behaves qualitatively similar to V_S .

Lagrangian tracking of aerosols as passive tracers shows how the complex flow pattern of the oblique wake allows some lucky aerosols to be entrained within the recirculating wake, resulting in a higher residence time within the highly supersaturated vortical zone. Importantly, We found that such a long residence time within the highly supersaturated wake not only exposes the aerosols to a higher level of supersaturation compared to its nucleation barrier, but also provides enough time for the growth by deposition of water vapor to exceed its critical size, and therefore to be activated as a CCN or INP. The frontal area of these lucky tracers entering the vortical but highly supersaturated oblique wake has a capture efficiency of $\sim 5 \times 10^{-3}$ with respect to the hydrometeor frontal area at $Re = 285$. Our analysis shows that wake-induced nucleation of aerosols during a convective precipitation of 20 minutes can generate $\mathcal{O}(10^3) - \mathcal{O}(10^6)\text{m}^{-3}$ new CCNs and INPs, which is in order of magnitude comparable to other secondary ice production mechanisms, and thus contribute to the life cycle of clouds.

Acknowledgments

This research was funded by the Marie - Skłodowska Curie Actions (MSCA) under the European Union's Horizon 2020 research and innovation programme (grant agreement no. 675675), and an extension to programme COMPLETE by Department of Applied Science and Technology, Politecnico di Torino. Scientific activities are carried out in Max Planck Institute for Dynamics and Self-Organization (MPIDS) and computational resources from HPC@MPIDS are gratefully acknowledged. First author wishes to acknowledge Giuliana Donini, Guido Saracco, Mario Trigiante and Paolo Fino for support.

References

- Adirosi, E., Volpi, E., Lombardo, F., & Baldini, L. (2016). Raindrop size distribution: Fitting performance of common theoretical models. *Advances in Water Resources*, *96*, 290 - 305. doi: 10.1016/j.advwatres.2016.07.010
- Bagchi, P., & Kottam, K. (2008). Effect of freestream isotropic turbulence on heat transfer from a sphere. *Physics of Fluids*, *20*(7), 073305. doi: 10.1063/1.2963138
- Baker, B. A. (1991). On the nucleation of ice in highly supersaturated regions of clouds. *Journal of the Atmospheric Sciences*, *48*(16), 1904-1907. doi: 10.1175/1520-0469(1991)048<1905:OTNOII>2.0.CO;2
- Baker, M. B. (1997). Cloud microphysics and climate. *Science*, *276*(5315), 1072-1078. doi: 10.1126/science.276.5315.1072
- Bhowmick, T., & Iovieno, M. (2019). Direct numerical simulation of a warm cloud top model interface: Impact of the transient mixing on different droplet population. *Fluids*, *4*(3).

- doi: 10.3390/fluids4030144
- Bodenschatz, E., Malinowski, S. P., Shaw, R. A., & Stratmann, F. (2010). Can we understand clouds without turbulence? *Science*, *327*(5968), 970–971. doi: 10.1126/science.1185138
- Chouippe, A., Krayer, M., Uhlmann, M., Dušek, J., Kiselev, A., & Leisner, T. (2019). Heat and water vapor transfer in the wake of a falling ice sphere and its implication for secondary ice formation in clouds. *New Journal of Physics*, *21*(4), 043043. doi: 10.1088/1367-2630/ab0a94
- Clift, R., Grace, J., & Weber, M. (1978). *Bubbles, drops, and particles*. Academic Press.
- Curtius, J. (2009). Nucleation of atmospheric particles. *Eur. Phys. J. Conferences*, *1*, 199–209. doi: 0.1140/epjconf/e2009-00921-0
- DeMott, P. J., Möhler, O., Cziczo, D. J., Hiranuma, N., Petters, M. D., Petters, S. S., ... Zenker, J. (2018). The fifth international workshop on ice nucleation phase 2 (fin-02): laboratory intercomparison of ice nucleation measurements. *Atmospheric Measurement Techniques*, *11*(11), 6231–6257. doi: 10.5194/amt-11-6231-2018
- Dusek, U., Frank, G. P., Hildebrandt, L., Curtius, J., Schneider, J., Walter, S., ... Andreae, M. O. (2006). Size matters more than chemistry for cloud-nucleating ability of aerosol particles. *Science*, *312*(5778), 1375–1378. doi: 10.1126/science.1125261
- Field, P. R., Lawson, R. P., Brown, P. R. A., Lloyd, G., Westbrook, C., Moisseev, D., ... Sullivan, S. (2017). Secondary ice production: Current state of the science and recommendations for the future. *Meteorological Monographs*, *58*, 7.1-7.20. doi: 10.1175/AMSMONOGRAPHS-D-16-0014.1
- Grabowski, W. W., & Wang, L.-P. (2013). Growth of cloud droplets in a turbulent environment. *Annual Review of Fluid Mechanics*, *45*(1), 293–324. doi: 10.1146/annurev-fluid-011212-140750
- Guo, Z., Zheng, C., & Shi, B. (2002). An extrapolation method for boundary conditions in lattice boltzmann method. *Physics of Fluids*, *14*(6), 2007–2010. doi: 10.1063/1.1471914
- Heymsfield, A., & Willis, P. (2014). Cloud Conditions Favoring Secondary Ice Particle Production in Tropical Maritime Convection. *Journal of the Atmospheric Sciences*, *71*(12), 4500–4526. doi: 10.1175/JAS-D-14-0093.1
- Huang, J. (2018). A simple accurate formula for calculating saturation vapor pressure of water and ice. *Journal of Applied Meteorology and Climatology*, *57*(6), 1265–1272. doi: 10.1175/JAMC-D-17-0334.1
- Huang, Y., Blyth, A. M., Brown, P. R. A., Choullarton, T. W., & Cui, Z. (2017). Factors controlling secondary ice production in cumulus clouds. *Quarterly Journal of the Royal Meteorological Society*, *143*(703), 1021–1031. doi: 10.1002/qj.2987
- Huffman, P. J. (1973). Supersaturation spectra of agi and natural ice nuclei. *Journal of Applied Meteorology*, *12*(6), 1080–1082. doi: 10.1175/1520-0450(1973)012<1080:SSOAAAN>2.0.CO;2
- Johnson, T. A., & Patel, V. C. (1999). Flow past a sphere up to a reynolds number of 300. *Journal of Fluid Mechanics*, *378*, 1970. doi: 10.1017/S0022112098003206
- Kanji, Z. A., Ladino, L. A., Wex, H., Boose, Y., Burkert-Kohn, M., Cziczo, D. J., & Krmer, M. (2017). Overview of Ice Nucleating Particles. *Meteorological Monographs*, *58*, 1.1-1.33. doi: 10.1175/AMSMONOGRAPHS-D-16-0006.1
- Kotou, M., Bouchet, G., & Duek, J. (2009). Transition to turbulence in the wake of a fixed sphere in mixed convection. *Journal of Fluid Mechanics*, *625*, 205248. doi: 10.1017/S0022112008005557
- Krayer, M., Chouippe, A., Uhlmann, M., Dušek, J., & Leisner, T. (2020). On the ice-nucleating potential of warm hydrometeors in mixed-phase clouds. *Atmospheric Chemistry and Physics Discussions*, *2020*, 1–21. doi: 10.5194/acp-2020-136
- Kreidenweis, S. M., Petters, M., & Lohmann, U. (2019). 100 Years of Progress in Cloud Physics, Aerosols, and Aerosol Chemistry Research. *Meteorological Monographs*, *59*, 11.1-11.72. doi: 10.1175/AMSMONOGRAPHS-D-18-0024.1
- Krüger, T., Kusumaatmaja, H., Kuzmin, A., Shardt, O., Silva, G., & Viggen, E. M. (2017).

- Lattice boltzmann method: Fundamentals and engineering applications with computer codes*. Springer, Cham. doi: 10.1007/978-3-319-44649-3_8
- Latt, J., Malaspinas, O., Kontaxakis, D., Parmigiani, A., Lagrava, D., Brogi, F., ... Chopard, B. (2020). Palabos: Parallel lattice boltzmann solver. *Computers & Mathematics with Applications*. doi: 10.1016/j.camwa.2020.03.022
- Lohmann, U. (2015). Aerosols — aerosolcloud interactions and their radiative forcing. In G. R. North, J. Pyle, & F. Zhang (Eds.), *Encyclopedia of atmospheric sciences (second edition)* (Second Edition ed., p. 17 - 22). Oxford: Academic Press. doi: 10.1016/B978-0-12-382225-3.00052-9
- McFiggans, G., Artaxo, P., Baltensperger, U., Coe, H., Facchini, M. C., Feingold, G., ... Weingartner, E. (2006). The effect of physical and chemical aerosol properties on warm cloud droplet activation. *Atmospheric Chemistry and Physics*, 6(9), 2593–2649. doi: 10.5194/acp-6-2593-2006
- Meyers, M. P., DeMott, P. J., & Cotton, W. R. (1992). New primary ice-nucleation parameterizations in an explicit cloud model. *Journal of Applied Meteorology*, 31(7), 708–721. doi: 10.1175/1520-0450(1992)031<0708:NPINPI>2.0.CO;2
- Michaelides, E. E. (2006). *Particles, bubbles and drops*. World Scientific. doi: 10.1142/6018
- Montgomery, R. B. (1947). Viscosity and thermal conductivity of air and diffusivity of water vapor in air. *Journal of Meteorology*, 4(6), 193–196. doi: 10.1175/1520-0469(1947)004(0193:VATCOA)2.0.CO;2
- Mossop, S. C. (1976). Production of secondary ice particles during the growth of graupel by riming. *Quarterly Journal of the Royal Meteorological Society*, 102(431), 45–57. doi: 10.1002/qj.49710243104
- Nair, V., Heus, T., & van Reeuwijk, M. (2020). Dynamics of Subsiding Shells in Actively Growing Clouds with Vertical Updrafts. *Journal of the Atmospheric Sciences*, 77(4), 1353–1369. doi: 10.1175/JAS-D-19-0018.1
- Prabhakaran, P., Kinney, G., Cantrell, W., Shaw, R. A., & Bodenschatz, E. (2020). High supersaturation in the wake of falling hydrometeors: Implications for cloud invigoration and ice nucleation. *Geophysical Research Letters*, 47(10), e2020GL088055. doi: 10.1029/2020GL088055
- Prabhakaran, P., Weiss, S., Krekhov, A., Pumir, A., & Bodenschatz, E. (2017). Can hail and rain nucleate cloud droplets? *Phys. Rev. Lett.*, 119, 128701. doi: 10.1103/PhysRevLett.119.128701
- Pruppacher, H. R., & Klett, J. D. (2010). *Microphysics of clouds and precipitation* (second ed.). Springer, Dordrecht. doi: 10.1007/978-0-306-48100-0
- Qian, Y., D’Humières, D., & Lallemand, P. (1992). Lattice BGK models for Navier-Stokes equation. *Europhysics Letters*, 17(6), 479–484.
- Rosenfeld, D., Zheng, Y., Hashimshoni, E., Pöhlker, M. L., Jefferson, A., Pöhlker, C., ... Andreae, M. O. (2016). Satellite retrieval of cloud condensation nuclei concentrations by using clouds as ccn chambers. *Proceedings of the National Academy of Sciences*, 113(21), 5828–5834. doi: 10.1073/pnas.1514044113
- Seinfeld, J., & Pandis, S. (2006). *Atmospheric chemistry and physics: From air pollution to climate change* (2nd ed.). John Wiley & Sons, New York.
- Siebert, H., & Shaw, R. A. (2017). Supersaturation fluctuations during the early stage of cumulus formation. *Journal of the Atmospheric Sciences*, 74(4), 975–988. doi: 10.1175/JAS-D-16-0115.1
- Silva, G., & Semiao, V. (2012). First- and second-order forcing expansions in a lattice boltzmann method reproducing isothermal hydrodynamics in artificial compressibility form. *Journal of Fluid Mechanics*, 698, 282303. doi: 10.1017/jfm.2012.83
- Stevens, B., & Bony, S. (2013). What are climate models missing? *Science*, 340(6136), 1053–1054. doi: 10.1126/science.1237554
- Succi, S. (2001). *Lattice Boltzmann equation for fluid dynamics and beyond*. Oxford: Clarendon Press.
- Tian, F.-B., Wang, Y., Liu, H., & Zhang, Y. (2018). The lattice Boltzmann method and its applications in complex flows and fluidstructure interactions. *Proceedings of*

- the Institution of Mechanical Engineers, Part C: Journal of Mechanical Engineering Science*, 232(3), 403–404. doi: 10.1177/0954406218754913
- Tomboulides, A. G., & Orszag, S. A. (2000). Numerical investigation of transitional and weak turbulent flow past a sphere. *Journal of Fluid Mechanics*, 416, 4573. doi: 10.1017/S0022112000008880
- Waldvogel, A. (1974). The N0 Jump of Raindrop Spectra. *Journal of the Atmospheric Sciences*, 31(4), 1067-1078. doi: 10.1175/1520-0469(1974)031<1067:TJORS>2.0.CO;2
- Wang, J., Krejci, R., Giangrande, S., Kuang, C., Barbosa, H. M. J., Brito, J., ... Martin, S. T. (2016). Amazon boundary layer aerosol concentration sustained by vertical transport during rainfall. *Nature (London)*, 539(7629). doi: 10.1038/nature19819
- Yuan, T., Martins, J. V., Li, Z., & Remer, L. A. (2010). Estimating glaciation temperature of deep convective clouds with remote sensing data. *Geophysical Research Letters*, 37(8). doi: 10.1029/2010GL042753